Analytical Methods

ROYAL SOCIETY OF CHEMISTRY

PAPER

View Article Online
View Journal

Cite this: DOI: 10.1039/d5ay01758k

Multi-detector frit-inlet asymmetric flow field-flow fractionation method development for nanoparticle mixtures: deeper analysis beyond ISO quality standards

Rand Abdulrahman, [a] Panida Punnabhum, [a] Lisa Van Den Driest,[a] Nicholas J. W. Rattray, [a] Robin Capomaccio, [b] Kevin Treacher, [b] Yvonne Perrie [a] and Zahra Rattray *[a]

Lipid-based nanoparticles (LNPs) are transforming the field of drug delivery, with one gene therapy product and four mRNA vaccines approved at the time of this report. As with other novel nanomedicines, the development of reliable and standardized methods for evaluating their quality attributes—factors that are essential for quality control and regulatory compliance—is essential to support their bench-to-bedside transition. Frit-Inlet Asymmetric Flow Field-Flow Fractionation (FI-AF4) combined with ultraviolet (UV), multi-angle light scattering (MALS) and dynamic light scattering (DLS) online detectors is widely recognized as a robust and versatile technique for the physicochemical analysis of LNPs. A robust protocol for FI-AF4 method development was established for a mixture of MC3-LNPs and bovine serum albumin (BSA), guided by preliminary particle size and polydispersity assessments using lower-resolution techniques such as DLS and nanoparticle tracking analysis (NTA). The FI-AF4 technique was subsequently applied to characterize particle size and morphology, and to evaluate the most suitable MALS fitmodels across different analytical approaches. The coupling of FI-AF4 with online MALS and DLS enabled the simultaneous separation and online analysis of large sub-populations contained in the sample (methods 2–4), which could not be detected using method 1. The change in particle morphology was found to be significant amongst different methods for each subpopulation (shape factor 0.709–0.793 for LNP peak 1, 0.765–0.853 for LNP peak 2, and 1.069–1.263 for LNP peak 3). MALS fit models indicate that the coated sphere and random coil models were the most appropriate fits for the three LNP sub-populations (R^2 > 0.95 and RMSE < 0.009). In summary, implementing the FI-AF4-UV-MALS-DLS protocol provided successful separation of LNPs from protein-containing media with additional analytical approaches not previously described by ISO guidelines. Collecting robust and reproducible information on LNP attributes is key to the several phases of drug development that ideally transform a drug in the pre-clinical phase, from bench-to-bedside.

Received 21st October 2025
Accepted 17th January 2026

DOI: 10.1039/d5ay01758k

rsc.li/methods

1 Introduction

Lipid nanoparticles (LNPs) have emerged in recent years as a promising nanocarrier-based delivery system for a diverse therapeutic payload, with several formulations incorporating small molecule drugs and nucleic acid-based drugs (*e.g.* siRNA and mRNA) against target therapeutic indications of unmet clinical needs. With such an acceleration in the industry uptake of LNPs, comes the need for analytical pipelines to profile their formulation and biological attributes. This need for novel analytical approaches has introduced challenges in the context of analytical method reliability and reproducibility due to the dynamic and complex nature of LNPs.

To date, there are four RNA LNP-based therapeutics on the market, siRNA drug Onpattro® (Alnylam Pharmaceuticals)[1] for the treatment of hereditary transthyretin-mediated amyloidosis (hATTR), three mRNA vaccines against SARS-CoV2, Spikevax® (Moderna),[2] mNEXSPIKE® (Moderna)[3] and Comirnaty® (Pfizer/BioNTech)[4] and the mRESVIA® (Moderna) mRNA vaccine against respiratory syncytial virus (RSV) in 2023.[5] The clinical success of these LNP-based therapeutics has drawn attention to the analytical methodologies used for the characterisation of these drug delivery systems.

LNPs are typically composed of four primary lipid components: (1) ionizable lipids that facilitate the encapsulation of

[a]*Strathclyde Institute of Pharmacy and Biomedical Sciences, University of Strathclyde, Glasgow, UK. E-mail: zahra.rattray@strath.ac.uk*

[b]*Global Product Development, Pharmaceutical Technology & Development, Operations, AstraZeneca, Macclesfield, UK*

negatively charged nucleic acid payload and promote endosomal escape, enabling cytosolic release of nucleic acid,[6] (2) helper lipids and (3) cholesterol, both of which support stability during storage and improve circulation time[7] and (4) polyethylene glycol (PEG)-conjugated lipids that prolong LNP circulation time by reducing opsonisation and clearance.[8]

While considerable research focus has been invested in establishing the role of each lipid in the LNP structure[7–12] and modulating LNP immunogenicity,[13–18] comparatively less attention has been given to the pre-clinical characterisation of LNPs using advanced analytical techniques. A major regulatory challenge lies in the accurate quantification of LNP-based formulation Critical Quality Attributes (CQAs). Comprehensive understanding and control of these CQAs is critical for successful translation, and the safety and efficacy of LNP-based products in clinical applications.

While suitable for a quality control setting, lower resolution techniques such as Dynamic Light Scattering (DLS) and Nanoparticle Tracking Analysis (NTA) offer limited information on LNP CQAs, including formulation heterogeneity, degradation, and morphology. These limitations necessitate the use of high-resolution orthogonal techniques that can generate reproducible data and detect subtle inter-batch variations. However, the high cost and complexity of these methods can be prohibitive. Compounding these issues is the current lack of regulatory guidelines and harmonization of analytics specifically tailored to LNPs, which contributes to inconsistency, ambiguities and a lack of standardization across analytical practices. At present, these gaps are being addressed by various institutions and initiatives (*e.g.* European Nanomedicine Characterisation Laboratory (EUNCL),[19] International Organization for Standardization (ISO),[20] American Society for Testing and Materials (ASTM),[21] SINTEF and LNE[22] and Joint Research Centre of the European Commission (JRC)).[23]

The application of Asymmetric Flow Field-Flow Fractionation (AF4) has recently gained prominence for evaluating the impact of manufacturing processes on LNP formulation attributes,[24] measuring particle size,[25–32] and profiling LNP nano-bio interactions.[30] AF4 multiplexed with online detectors can simultaneously perform separation and analysis of sub-populations within a polydisperse sample. By virtue of its low shear stress in comparison to chromatographic approaches, AF4 is a non-disruptive and powerful separation technique widely used for the analysis of nanomedicine physicochemical attributes.[25–32] In principle, analytes are introduced into the AF4 channel and concentrated on the accumulation wall. An external force field is applied perpendicular to the parabolic flow of the channel mobile phase, resulting in size-based separation under diffusion.[33]

Unlike traditional chromatographic methods, the absence of a stationary phase compared to traditional chromatographic techniques and lower system pressures, offers a minimally disruptive means of separating polydisperse nanoparticle mixtures due to a lack of nanoparticle adsorption on the stationary phase in chromatography columns, and minimal high shear forces. This gentle separation allows for the analysis of complex nanoparticle mixtures that are otherwise challenging to analyse using conventional techniques.[34]

Two main modalities of AF4 are commonly employed, conventional AF4 (hereafter referred to as AF4) and frit-inlet AF4 (FI-AF4). AF4 was first introduced in the 1980s by Giddings and Wahlund[35] followed by the later introduction of FI-AF4.[36] The FI modality is integrated into AF4 platforms with the main aim of mitigating the focusing step and improving the resolution for sensitive samples.[36,37] Conventional AF4 requires a focusing step, in which a dedicated focus flow is applied to concentrate the sample at the head of the channel and establish a steady-state distribution. However, this focusing period can promote sample loss through interactions with the accumulation wall membrane or induce particle agglomeration.[38,39] FI-AF4 eliminates the need for a focus flow. Instead, the sample undergoes hydrodynamic relaxation as it enters the channel through the porous frit.[40] Sample localisation is achieved by two opposing flows (downstream channel flow and perpendicular cross-flow, without the use of a focusing step). This reduces the direct exposure of particles to the membrane, minimising sample loss and agglomeration.[30,40–42] A further advantage of using FI-AF4 is the ability to use a higher injection mass while minimising the overloading effect.[37] Conventional AF4 may prevent the complete relaxation of the samples into the channel due to the focusing step resulting in an overloading effect.[43] FI-AF4-DLS has also been shown to provide enhanced resolution for the characterisation of dextran nanoparticles.[41] Comparable elution profiles have been reported between AF4 and FI-AF4 for the separation of nAg-extracellular polymeric substances (EPS)[44] and improved recovery of LNPs using FI-AF4-MALS.[40] However, Fuentes *et al.* reported poor subpopulation resolution with FI-AF4 compared to AF4.[37] Importantly, FI-AF4 is not widely and commercially available in laboratories. The preferred approach therefore depends on both the analytical priorities (aggregation, sample–membrane interaction, resolution and recovery) and on modality availability.

Method development for AF4 remains a complex and nuanced process, requiring the careful optimisation of many parameters, including the choice of membrane, selection of the appropriate cross-flow, focus flow (AF4), and detector flow rates, choice of channel geometry and dimensions, accounting for sample surface charge characteristics, sample injection volume and composition of the carrier liquid. Despite the growing interest in AF4, there is a distinct lack of method development literature on AF4 applications for LNP separation and analysis,[34] where publishing method development protocols can significantly benefit the community in implementing robust and reproducible pipelines for profiling nanomedicines during early discovery efforts.

The International Organization for Standardization/Technical Specification ISO/TS 21362:2021 guideline 'Nanotechnologies – Analysis of nano-objects using asymmetrical-flow and centrifugal field-flow fractionation' addresses the requirements of analytical characterisation of nanomaterials using AF4.[20] While this guideline addresses most nanomaterials, its practical application for complex nanoparticle mixtures due to their inherent polydisperse nature is often challenging. Moreover, there is considerable variation in the published literature on what constitutes a 'satisfactory' AF4 method, with one such

example being the satisfactory relative standard deviation (RSD) between replicate runs, the threshold for acceptable resolution and context-dependent percentage sample recovery. Resolution is defined as "two adjacent eluting peaks representing two monodisperse populations"; however the presence of polydisperse populations hinders the calculation of the resolution factor.[20] The key contribution of this work is the development of the FI-AF4 protocol that directly addresses several limitations in the current ISO/TS 21362:2021 guideline. The FI-AF4 protocol demonstrated improved run-to-run repeatability and provided superior resolution of polydisperse populations in the sample, enabling the accurate separation and characterisation of subpopulations that may be overlooked by the current available guidelines. The protocol also incorporates MALS fit model reporting, ensuring that the assumption and parameters used in data interpretation are reproducible and comparable across repeated studies. In addition, the FI-AF4 protocol addresses the occurrence of sample recoveries of >100%, which are not addressed by previous FI-AF4 guidelines leaving uncertainty in data interpretation. Hence, the parameters established in this work represent the best practices that can serve as a foundation for future FI-AF4 guidelines and standardisation efforts.

Multiple detectors can be multiplexed with FI-AF4 to measure nanoparticle CQAs, that include MALS[29,40,45] (measuring the radius of gyration (R_g) and molecular weight), UV[44,46–50] and refractive index (RI) (measuring concentration)[30,42,48,51–56] and DLS (measuring the hydrodynamic radius (R_h)).[32,47,52,57–60] Particle structure and morphology can be inferred from combining the readout from both MALS and DLS detectors and obtaining R_g/R_h.[41,48,55,56,61,62] Differences in the R_g/R_h ratio provide insights into nanoparticle geometry, with values near 0.77 indicative of an ideal hard sphere,[63] whereas a shape factor value of ~1.22 suggests a rod-like geometry.[64] Particle morphology is essential for quality control as it reveals the presence of aggregates in the formulation, a factor that strongly influences product stability and LNP potency.[65,66] Analysis of MALS data requires a consideration of various experimental parameters, including the light scattering angles selected and the fit models applied to each sample component. Furthermore, theoretical model fits for optimal approximation of R_g remain limited in the literature. It becomes questionable whether calculation of R_g and R_g/R_h is a correct approximation in the absence of using optimal scattering angles and a lack of standardisation of fit models. Such unpublished details and key parameters of FI-AF4 analysis may hamper interlaboratory harmonisation efforts in standardising FI-AF4 analytical pipelines for nanomedicines.[43]

Sample recovery is a critical parameter in FI-AF4 to ensure the accurate quantification and representative characterisation of the analyte. ISO/TS 21362 recommends a recovery of >70% as acceptable for nanoscale particles. While this metric refers to the sample recovery of the entire sample, selecting a single appropriate detection wavelength becomes challenging for heterogeneous samples, particularly when various sample components absorb light at different wavelengths (*e.g.* nucleic acids and proteins absorb light at 260 nm and 280 nm, respectively).[67,68] Sample loss may arise from poor selection of membrane pore size as molecules may penetrate through the pores, attractive interactions occurring between the sample and the membrane, retention within tubing or channel edges, and solvent incompatibility. Conversely, inadequate method optimisation can lead to apparent recoveries of >100% due to mass overloading.[69–71]

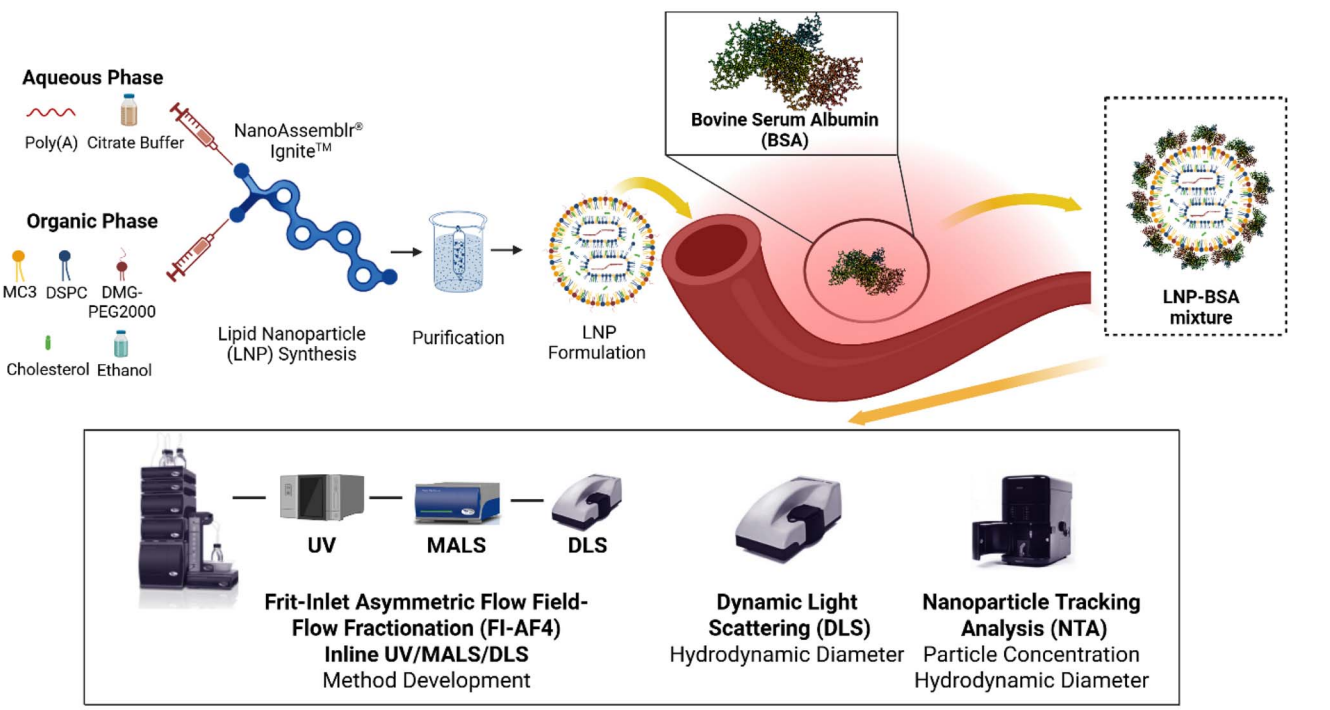

Fig. 1 Schematic procedure of MC3-LNPs synthesis, formation of the LNP–BSA mixture and characterisation using DLS, NTA and FI-AF4 coupled to ultraviolet (UV), multi-angle light scattering (MALS) and DLS detectors.

The focus of this work is to develop different FI-AF4 methods for a sample containing a mixture of different nanoparticle classes with different cross-flow and detector flow parameters (Fig. 1). We used three detectors (UV, MALS and DLS) to provide detailed FI-AF4 analysis. The selection criteria used in method development were based on minimal overlap between peaks, acceptable signal intensity (distinguishable analyte peak from baseline noise), sample recovery (>70%) and optimal fit to MALS scattering fit models (R^2 > 0.9 and root mean square error (RMSE) < 1). The data generated will complement the ISO/TS 21362:2021 method performance criteria for FI-AF4 method development on heterogeneous samples. The sample mixture used for FI-AF4 data analysis consists of LNPs and bovine serum albumin (BSA). This mixture was used since the nature of the nanoparticles is different; hence the FI-AF4 respective analysis in the case of nanoparticle mixtures is explained.

2 Methodology

2.1 Materials

Polyadenylic acid (poly(A)), cholesterol, sodium citrate dihydrate, ethanol, and a dialysis tubing cellulose membrane (molecular weight cut-off size 14 kDa) were purchased from Sigma-Aldrich (St. Louis, MO, USA). Helper lipids 1,2-distearoyl-*sn-glycero*-3-phosphocholine (DSPC) and 1,2-dimyristoyl-rac-*glycero*-3-methoxypolyethylene glycol-2000 (DMG-PEG 2000) were purchased from Avanti Polar Lipids (Alabaster, AL, USA). The ionisable lipid (6*Z*,9*Z*,28*Z*,31*Z*)-heptatriaconta-6,9,28,31-tetraen-19-yl-4-(dimethylamino)butanoate (D-Lin-MC3-DMA) was purchased from BroadPharm (San Diego, CA, USA). Lyophilised powder Bovine Serum Albumin (BSA), Invitrogen™ UltraPure™ DNase/RNase-Free Water and phosphate-buffered saline (PBS) 10× salt solution pH 7.4 were acquired from Fisher Scientific (Loughborough, UK).

2.2 Manufacture of lipid nanoparticles

Poly(A) LNPs were manufactured using a NanoAssemblr® Ignite Precision NanoSystems (Vancouver, BC, Canada) using a NxGen microfluidic cartridge. Lipid stocks were prepared in ethanol at a molar ratio of 50 : 38.5 : 10 : 1.5 for D-Lin-MC3-DMA : Cholesterol : DSPC : DMG-PEG 2000, which is based on the lipid compositions of Onpattro® and Comirnaty®.[30] The aqueous phase consisted of initial poly(A) stock at 1.5 mg mL^{-1} dissolved in 50 mM citrate buffer (pH 4.0). The N : P ratio was (N for lipid nitrogen and P for nucleic acid phosphate) was 6 : 1. The total flow rate (TFR) was set at 15 mL min^{-1}, and an aqueous-to-organic flow rate ratio (FRR) of 3 : 1 was used with a final lipid concentration of 1.25 mg mL^{-1} and poly(A) of 0.055 mg mL^{-1}. The resultant suspension was dialysed at 4 °C (14 kDa molecular weight cut-off (MWCO), Sigma-Aldrich, St. Louis, MO, USA) into 1× PBS (pH 7.4) (500× dialysate ratio) to remove ethanol and citrate buffer. LNP formulations were filtered through a 0.2 μm pore-sized Supor® membrane (Pall Corporation, USA), and stored at 4 °C until further use.

2.3 Sample preparation

LNP formulations were incubated with BSA to form an LNP–BSA mixture. LNPs were incubated at a 1 : 1 (volumetric ratio) with BSA (35 mg mL^{-1} in PBS, representing physiologically relevant albumin levels) for 24 hours at 37 °C. The control sample included an equal volume of PBS and LNPs.

2.4 Analysis of lipid nanoparticle properties

2.4.1 Dynamic light scattering (DLS) and electrophoretic light scattering (ELS) measurements. LNP formulation sample attributes were analysed using a Zetasizer Nano ZS (Malvern Panalytical, Malvern, Worcestershire, UK) to obtain the particle size and polydispersity index (PDI) for LNPs (LNP in PBS) at the 0 hour-time point (control) and control (LNP–PBS) and treated (LNP–BSA) at the 24 hour-time point. All measurements were performed using non-invasive backscattering (NIBS, 173°) at a dilution of 1:10 in PBS (pH 7.4). The refractive index (RI) and viscosity of the dispersant (PBS) were set at 1.34 and 1.02 cP, respectively. To measure the ζ-potential, ELS of the LNP-control was measured using the Smoluchowski approximation. All measurements were performed at a dilution of 1:10 in DNA/RNA free water. The RI and viscosity of the dispersant (DNA/RNA free water) were set at 1.33 and 0.89 cP, respectively. DLS and ELS measurements were performed at a measurement temperature of 25 °C, and material RI and absorbance were set at 1.45 and 0.001, respectively. All measurements were performed in three independent measurements consisting of at least three technical replicates.

2.4.2 Nanoparticle tracking analysis (NTA). NTA was used to perform *in situ* analysis of LNPs incubated with BSA, studying changes in LNP size in response to BSA surface-adsorption. All NTA measurements were performed using a NanoSight NS300 system (Malvern Panalytical, Malvern, Worcestershire, UK), configured with a 488 nm laser and a sCMOS camera. LNP samples were diluted in PBS (pH 7.4), and analyzed with the syringe driver set at 50. All measurements were performed at ambient temperature with five successive videos of 60 second duration captured, with a camera level of 14 and a detection threshold of 5 for all measurements. Particle dilutions were by a factor of 2 × 10^3. The mean and standard deviation for parameters were determined from three independent measurements consisting of five technical replicates.

2.4.3 Encapsulation efficiency (EE). Quant-iT™ RiboGreen RNA Assay (Invitrogen™, Thermo Fisher Scientific, UK) was used for the quantification of poly(A) encapsulation in LNPs as per manufacturer's instructions.

LNPs were serially diluted in tris and ethylenediaminetetraacetic acid (TE buffer) in the presence and absence of 2% v/v Triton X-100 in a 96-well plate. The plate was incubated at 37 °C for 15 minutes, followed by the addition of two dilutions of 1× Ribogreen Reagent (500- and 200-fold) to wells containing TE buffer and Triton X-100, respectively. Fluorescence was measured using a GloMax® Microplate Reader (Promega Corporation, UK) with an excitation of 475 nm and emission 500–550 nm wavelength. EE was calculated using the following equation:

$$\text{EE } (\%) = \frac{\text{poly(A)}_{\text{total}} - \text{poly(A)}_{\text{free}}}{\text{polyA}_{\text{total}}} \times 100 \quad (1)$$

where $\text{poly(A)}_{\text{total}}$ is the total poly(A) concentration ($\mu g\ mL^{-1}$) in wells containing triton–TE buffer and $\text{poly(A)}_{\text{free}}$ is the concentration ($\mu g\ mL^{-1}$) of the unentrapped poly(A) in wells containing TE buffer.

2.4.4 Frit-inlet asymmetric flow field-flow fractionation (FI-AF4). FI-AF4 measurements were carried out as previously described by Abdulrahman *et al.*[30] A Postnova Analytics AF2000 AF4 (Landsberg, Germany) was used to separate LNP-BSA. The system was configured with three online detectors, a (1) UV (PN3242, 260 nm-Postnova Analytics), (2) Multi-angle Light Scattering (MALS-PN3621, Postnova Analytics), and Zetasizer Nano ZS (Malvern Panalytical, Malvern, UK). Separation was performed using a frit-inlet rectangular channel (300 × 60 × 40 mm) assembled with a trapezoidal geometry, (spacer thickness 350 μm). An amphiphilic regenerated cellulose (RC) membrane with a 10 kDa MWCO was used, with a 100 μL injection loop and 20 μL sample injection volume. PBS (10 mM at pH 7.4) was used as the carrier liquid. Online DLS measurements were performed using a Malvern quartz flow cell (ZEN0023) with a flow rate of 0.2 mL min^{-1} and data collected every 3 seconds. The temperature was set at 25 °C. The measurement position was fixed at 4.2 mm, and the attenuator was set to 11.

FI-AF4 method development included the optimisation of detector flow, and exponential decay cross-flow. A total of four methods were simulated (Table 1 and SI Fig. S1 and S2). Method development was initiated with the LNP–BSA incubated sample at the 24-hour time-point to determine separation efficiency of the two sub-populations. Method development was based on the flowchart in Fig. 2.

The recovery (R%) of the samples for each method was calculated using the following equation:

$$R\ (\%) = \frac{A_c}{A} \times 100 \quad (2)$$

where A_c is the area under the peak of nanoparticles under a cross-flow, and A is the area under the peak of the unfractionated sample without an applied cross-flow *via* direct sample injection. Absorbance was compared between 260 nm and 280 nm wavelengths using a UV detector. Aggregates eluting after the cross-flow stops were not included in fractogram integration. The percent recovery was calculated for run-to-run triplicates. A criterion to establish the optimal methodology was based on a sample recovery of >70%.

The MALS detector was normalized using BSA and a laser power set to 80%. Four different model fit transformations for light scattering (Zimm, coated sphere, random coil and Debye) were examined for extracting the R_g based on the data obtained from Nova FFF software (version 2.2.0.1, Postnova Analytics, Landsberg, Germany). The Zimm model assumes isotropic scattering from small particles (R_g < 50 nm), best suited from near-spherical nanoparticles as the model assumes angular dependence is minimal.[19] The coated sphere model accounts for a dense core surrounded by a shell-layer. The Debye model describes the scattering from Gaussian random coils and is particularly applicable for flexible polymers or proteins.[72] The random coil model is an extension of the Debye model. While the Debye model uses a polynomial function, the random coil model fits the angular light scattering data using the formula for a theoretical random coil.[19]

The normalised root mean square error (RMSE) and coefficient of determination (R^2) were obtained using Python 3.12.4 by comparing the actual and the predicted values for the model from the slope (R_θ/K_c against $\sin^2(\theta/2)$ plot) for the predicted values. The actual and predicted values were obtained from Nova FFF software. Curve fitting was performed using scattering angles between 36° and 148° for all methods investigated.

Shape factor measurements were calculated using the equation below:[73]

$$\rho = \frac{R_g}{R_h} \quad (3)$$

where ρ is the shape factor, R_g represents the radius of gyration (nm) obtained from the MALS detector, and R_h represents the hydrodynamic radius (nm) obtained from the DLS detector.

2.5 Statistical analysis

Statistical analysis was performed with one-way ANOVA followed by Tukey's multiple comparisons test for post-hoc analysis. Statistical significance was considered at p-value < 0.05; *p < 0.05, **p < 0.01, ***p < 0.001, and ****p < 0.0001. All data were

Table 1 Corresponding FI-AF4 parameters for the four methods. Reader is referred to SI Fig. S1 for simulated methods on NovaAnalysis software

Method	Time (min)	Cross-flow (mL min^{-1})	Type	Exponent	Detector flow (mL min^{-1})
1	20	0.75	Constant	0	0.2
	60	0.75	Power	0.2	
	10	0	Constant	0	
2	20	1.0	Constant	0	0.2
	60	1.0	Power	0.2	
	10	0	Constant	0	
3	20	1.5	Constant	0	0.2
	60	1.5	Power	0.2	
	10	0	Constant	0	
4	20	1.5	Constant	0	0.3
	60	1.5	Power	0.2	
	10	0	Constant	0	

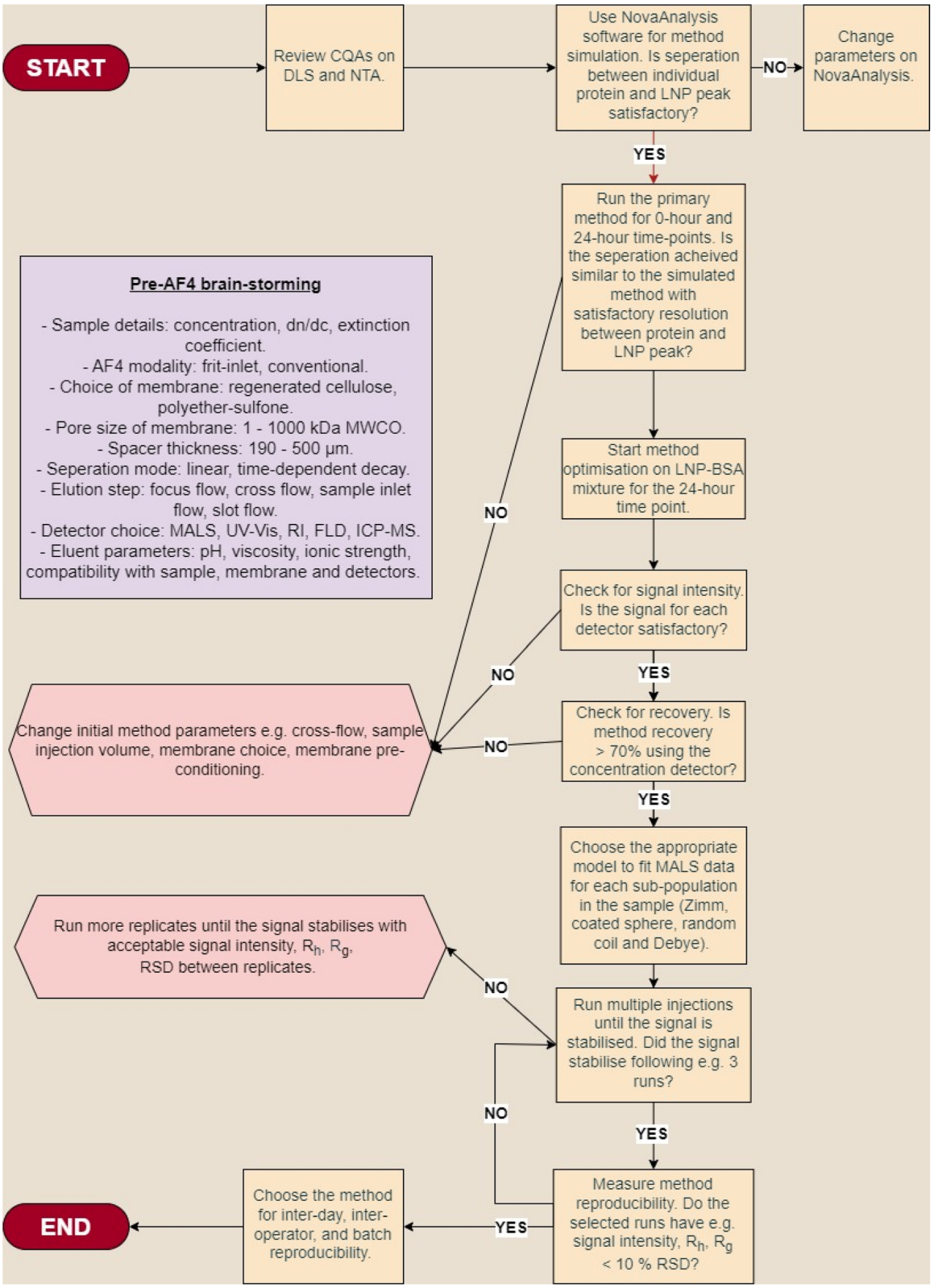

Fig. 2 Protocol adopted for method optimisation on FI-AF4 for nanoparticle mixtures. Abbreviations: FLD, fluorescence detector, ICP-MS, inductively coupled plasma mass spectrometry, and RSD, relative standard deviation. Method performance criteria used for the selection of the optimal method were guided by the ISO/TS 21362:2021 standards.[20] Criteria included a recovery (*R*%) of >70, retention $0.03 \leq R \leq 0.2$ and resolution $R_s > 1.5$ in the case of a Gaussian peak and non-overlap peaks in the case of non-Gaussian peaks.

analyzed using GraphPad Prism 9.5.1 (GraphPad Software Inc.) and are expressed as mean ± SD ($n = 3$) or stated otherwise.

3 Results and discussion

3.1 Physicochemical characterisation using DLS and NTA for initial batch-mode characterisation

The CQAs of the MC3-LNP formulation are shown in Table 2. LNPs were incubated with BSA and examined for their particle diameter using distribution algorithm analysis, size distribution profile, polydispersity and particle concentration. Initial LNP CQAs were measured using DLS (*Z*-average and PDI), ELS (zeta potential) and EE before corona formation with BSA and fractionation using FI-AF4. LNPs manufactured had a mean *Z*-average of 75.9 (±4.6) nm, a PDI < 0.2 and a zeta-potential of −3.6 (±4.2) mV. The EE in all cases was measured to be >95%.

Table 2 Baseline critical quality attributes (CQAs) for MC3-LNPs. The *Z*-average and polydispersity index (PDI) were measured using DLS cumulant algorithm analysis. *Z*-average is described for the hydrodynamic particle diameter. Zeta potential was measured by electrophoretic light scattering (ELS). Poly(A) encapsulation efficiency was measured using the RiboGreen™ RNA assay. Data are shown as mean ± SD, $N = 3$

DLS parameters	MC3-LNP
Z-average (nm)	75.9 (±4.6)
PDI	0.152 (±0.039)
Zeta potential (mV)	−3.6 (±4.2)
Encapsulation efficiency (%)	98 (±2)

Following LNP incubation with BSA, the different sub-populations could not be compared using the *Z*-average cumulant analysis due to the high PDI of 0.540 (±0.049) on DLS and a span of 0.61 (±0.04) using NTA (Fig. 3) occurring as a result of excess unadsorbed BSA contained in the incubation media (peak 1). Comparing particle size distribution for the BSA-control and the LNP-control to the LNP–BSA mixture, peak 1 and peak 2 occurring at a particle diameter of 7.5 (±0.2) nm were identified as free BSA, and peak 2 at a particle diameter of 92.7 (±2.9) nm were identified as free BSA (BSA-control) and LNPs bound to BSA (LNP–BSA) respectively (Fig. 3A and SI Table S2). Peak 3 for all samples (BSA-control 0-hour, LNP-control 0-hour and 24-hour and LNP–BSA 24-hour) are defined as aggregates.

Size measurements by NTA followed a similar trend to that of DLS. Comparing changes in the NTA-measured LNP–BSA complex, concentration distribution profiles did not show distinct peaks corresponding to BSA and LNPs; however they

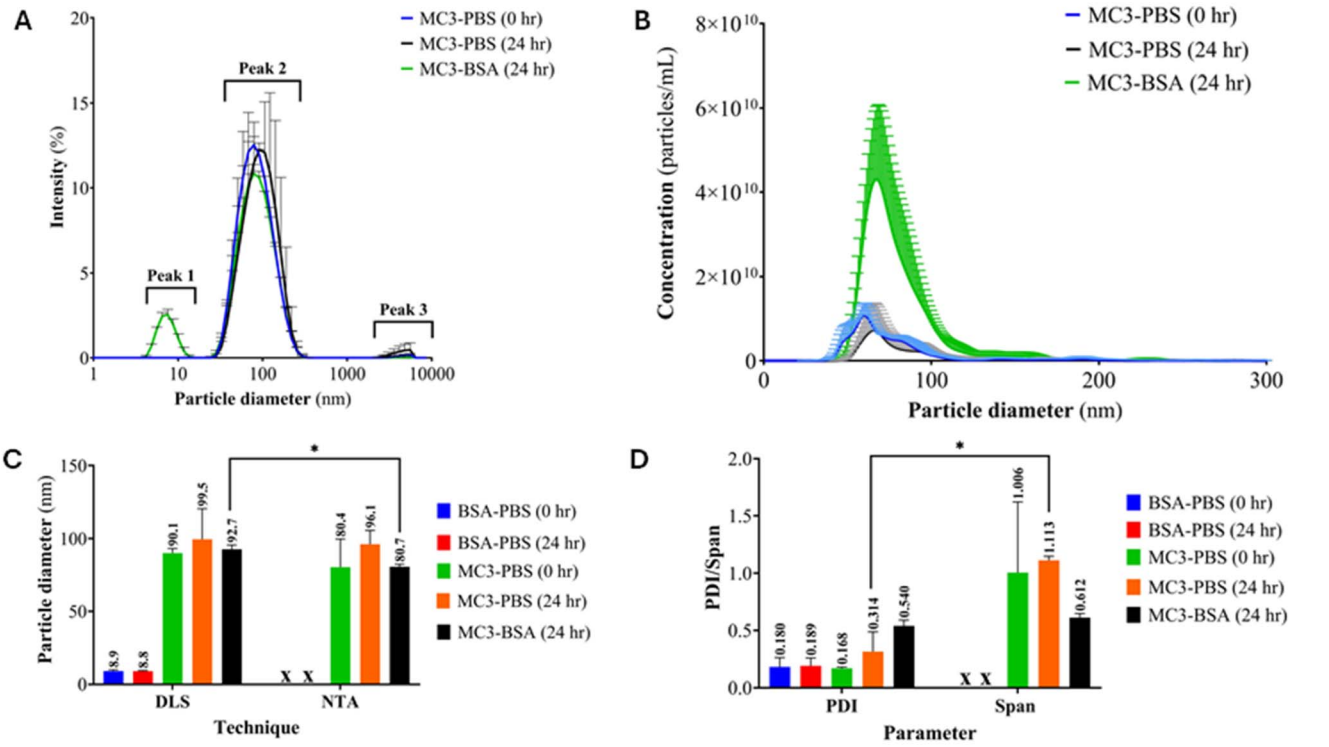

Fig. 3 Particle size analysis using DLS and NTA for MC3-LNPs incubated in PBS (control) and 35 mg mL^{-1} bovine serum albumin (BSA) at 0 hours (control) and 24 hours incubation at 37 °C. Plots represent (A) particle size distribution by DLS cumulative algorithm analysis, (B) NTA particle size distribution, (C) comparison of the particle diameter obtained using DLS and NTA and (D) the polydispersity index (PDI) measured by DLS and span using NTA, calculated as $(D_{90} - D_{10})/D_{50}$. DLS data were measured by cumulant algorithm analysis for intensity-weighted mean particle size. Results are shown as mean ± SD, $n = 3$. 'X' in plots (C) and (D) refers to samples not measured due to the polydispersity of the BSA and LNP mixtures for DLS. Peak 1 indicates the BSA peak, peak 2 indicates LNP peaks and peak 3 refers to aggregate particles. *$p < 0.05$ as determined by a two-tailed paired *t*-test.

showed a polymodal size distribution (Fig. 3B). An increase in concentration resulted from 2.4×10^{11} ($\pm 2.0 \times 10^{11}$) particles/mL (LNP–PBS at 24-hour) to 1.4×10^{12} ($\pm 5.9 \times 10^{11}$) particles/mL, which is attributed to the presence of BSA. The incubation of LNPs with BSA for 24 hours resulted in a shift in the mean particle diameter to 96.1 ($\pm$9.4) nm for LNP-control and 80.7 ($\pm$1.8) nm for LNP–BSA.

3.2 Optimisation of FI-AF4 parameters for the separation of LNP–BSA complexes from bulk incubation media

The superior separation power of FI-AF4 allows for the high-resolution separation of free BSA from LNP–BSA corona complexes, which was otherwise difficult to measure using batch-mode DLS and NTA due the highly polydisperse nature of these mixtures. Multi-detector hyphenation enabled determination of the signal intensities, particle size and morphology (combining DLS and MALS detectors to measure R_g/R_h) for the different particle sub-populations within these complex mixtures. FI-AF4 method development increases in complexity with mixtures of heterogeneous nanoparticles with varying material compositions.

Here, we used MC3-LNPs and BSA in the mixture to form MC3-BSA corona complexes (BSA was present in excess concentration at a physiologically relevant concentration of 35 mg mL^{-1}), followed by the separation of free BSA from the MC3-BSA corona. The cross-flow (0.75, 1 and 1.5 mL min^{-1}), detector flow (0.2 and 0.3 mL min^{-1}) and UV detector wavelength (260 nm and 280 nm) were varied between methods, while maintaining all other run parameters constant. Ideally, the fractograms for the different detectors exhibit a narrow Gaussian distribution and minimal overlap between free BSA and LNP–BSA corona complex peaks. Prior to method optimisation, the control for BSA and LNPs were carried out using method 1 to identify and assign peaks accurately (SI Fig. S3). Each fractogram shows an initial BSA peak eluting at ~5 min, followed by two LNP sub-populations, LNP peak 1 and peak 2 eluting after 20 min.

3.2.1 Analysis of LNPs using FI-AF4-UV. The intensity of the BSA and LNP UV signals was measured at 280 nm and 260 nm,

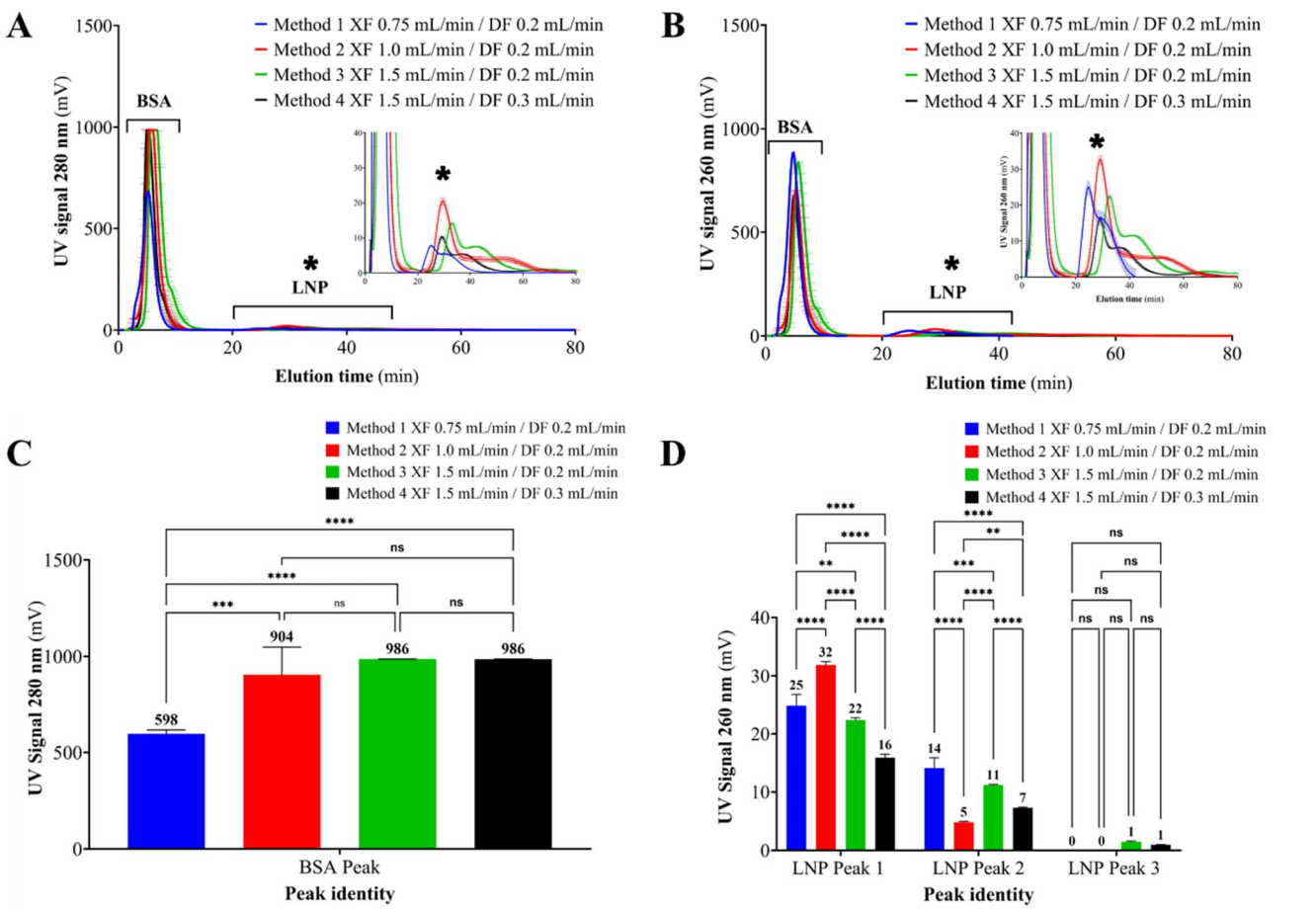

Fig. 4 The use of a UV detector coupled to FI-AF4 for determining the differences between signal intensities between methods 1–4 with different cross-flow rates (XF) and detector flow rates (DF). Plots represent MC3-LNPs incubated in 35 mg mL^{-1} bovine serum albumin (BSA) at 37 °C for 24 hours. (A) FI-AF4-UV fractogram profile at 280 nm and (B) 260 nm (C) signal intensities measured for UV detection at 280 nm and (D) 260 nm. Error bars represent ± SD mean of triplicate injections. The peaks marked with asterisks (*) show enlarged peaks. Statistical analysis was performed using one-way ANOVA followed by post-hoc Tukey's test. *$p < 0.05$, **$p < 0.01$, ****$p < 0.0001$, and ns non-significant. Refer to SI Fig. S4 for BSA and LNP peaks 1–3 identifications.

respectively (Fig. 4). Fig. 4A and B present a well-defined peak for BSA (eluting at ~5 min). The LNP shows different sub-populations eluting at different time-points in the UV fractogram elution profile. Fig. 4A and B show that the measured signal for BSA is ~50-fold higher than that of LNPs. The increased signal for BSA at 280 nm is attributed to tryptophan (Trp) and tyrosine (Tyr) residues, which absorb at 280 nm.[74] LNP absorbance at 260 nm is attributed to the aromatic chromophore of the aromatic base adenine in the mRNA (poly(A)) encapsulated in the LNP.[34]

Methods 1, 2 and 3 were run at progressively higher cross-flow (0.75, 1.0 and 1.5 mL min^{-1} respectively); however this did not result in a consistent increase in elution time across all sub-populations within the sample. Method 1 had two LNP sub-peaks eluting without sufficient resolution at 25.5 (±0.1) min (peak 1) and 32.5 (±0.5) min (peak 2) (Fig. 4B). The higher cross-flow applied in method 2 eluted the first LNP subpopulation at 30 (±0.1) min and the second subpopulation at 53.5 (±0.3) min. However, methods 3 and 4 produced the longest elution times for the first LNP sub-population, with method 3 yielding 33.2 (±0.1) min and a shorter elution time for method 4 for the same sub-population (29.5 (±0.1) min). The UV absorbance for LNPs arises from the encapsulated nucleic acid (poly(A)), which may be distributed unevenly across the elute fractions. Hence, LNP peak 3 can be identified as larger LNPs (due to a longer elution time). However, a lower intensity for LNP peak 3 might indicate that the poly(A) content encapsulated per particle is lower or might have leaked from the LNPs when the aggregates formed or during the elution time period of the method. Methods 3 and 4 exhibited substantial tailing and fractionated larger sized particles in the sample.

In FI-AF4, increasing the cross-flow rate (while maintaining other parameters constant) decreases the detector signal intensity. This trend was not observed for BSA and LNP peaks (Fig. 4C and D). Increasing the cross-flow rate from 0.75 mL min^{-1} to 1.0 mL min^{-1} increased the signal intensity from 598 (±0)% to 986 (±0)% (Fig. 4C and D). This can be attributed to the saturated peak intensity shown by the peak capping in methods 2 and 3 due to the BSA concentration (35 mg mL^{-1}) used. The LNP peaks showed statistically significant differences in intensities across all four methods, both for LNP peak 1 and LNP peak 2 with no statistical significance in the case of LNP peak 3. Statistically significant differences were observed between intensities measured across all four different methods (LNP peak 1 and LNP peak 2) (Fig. 4D).

3.2.2 Method repeatability. The repeatability of the cross-flow profile for each method was tested by three replicate injections under identical conditions (SI Fig. S4 and SI Table S3), and the RSD of UV signal intensity was calculated for each method for a polydisperse sample (LNP–BSA mixture).

Fig. 5 illustrates the RSD of peak intensities across the four FI-AF4 methods. Method 4 had the lowest RSD for LNP peaks 1–3 (1–4%). Method 1 showed a clear trend in increased RSD with higher particle size (3–13%). Method 2 showed the highest variability for the BSA peak (16%) indicating low injection precision for the protein. In the case of LNP peaks, methods 1 and 3 exhibit signal intensities (>5%) between replicate injections, whereas methods 2 and 4 maintain variability within the

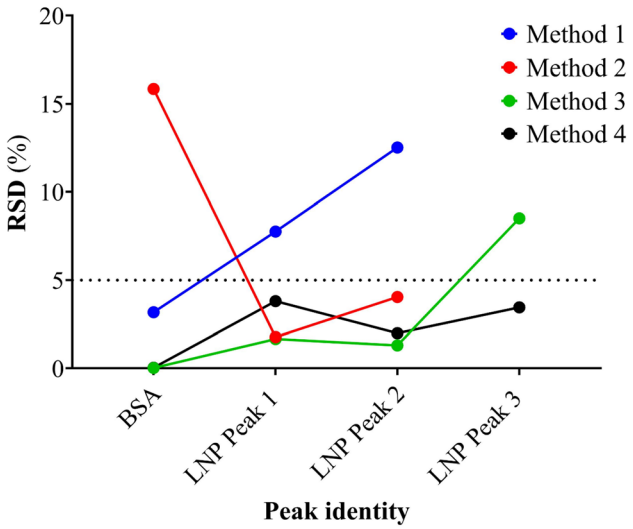

Fig. 5 Relative standard deviation (RSD%) of UV signal intensities of the LNP–BSA sample across three replicate runs for four FI-AF4 methods. The signal intensities were measured using the UV detector at 260 nm and 280 nm wavelengths for MC3-LNPs and BSA, respectively. Refer to SI Fig. S4 for FI-AF4-UV fractograms for peak identification and run-to-run replicates and SI Table S3 for signal intensities of methods 1–4 at UV 260 and 280 nm. The dotted horizontal line indicates 5% RSD.

acceptance criteria of ISO/TS 21362 (<5%). These findings demonstrate that increasing the cross-flow rate (0.75–1.5 mL min^{-1}) does not inherently enhance run-to-run repeatability, and in some cases may contribute to variability. An optimized cross-flow to detector-flow ratio (method 4) contributed to consistent retention behaviour for each component in the sample across three replicate runs.

3.2.3 Contribution of the UV detector at 260 nm and 280 nm signal intensity for percentage sample recovery. The presence of analyte mixtures with different optical characteristics (*i.e.* BSA and LNPs) renders the quantification of sample recovery at a single UV detector wavelength challenging. Method 3 exhibited a more prominent truncation of the BSA peak relative to the other methods, while method 4 showed incomplete elution of LNP peak 3 (SI Fig. S4), resulting in non-representative recovery data. Therefore, methods 1 and 2 were selected for determining sample recovery. Methods 1 and 2 achieved an acceptable sample recovery level of >70%. Method 1 resulted in no statistically significant differences in recovery determined using 260 nm and 280 nm (105% for 260 nm and 96% for 280 nm) detection wavelengths, but a significant difference was noted for method 2 (102% for 260 nm and 127% for 280 nm) (Fig. 6 and SI Fig. S5). An increased concentration of the sample can improve detection using FI-AF4 but can also cause overloading (recovery of >100%). Marioli *et al.* observed higher retention times, peak broadening, and fronting peaks with overloaded fractograms.[43] To mitigate these artefacts, samples should be diluted to fall within the lower and upper limits of the detector with sample loading to be adjusted to avoid channel saturation. The type of protein, membrane protein permeability,[43] carrier liquid composition,[43] spacer

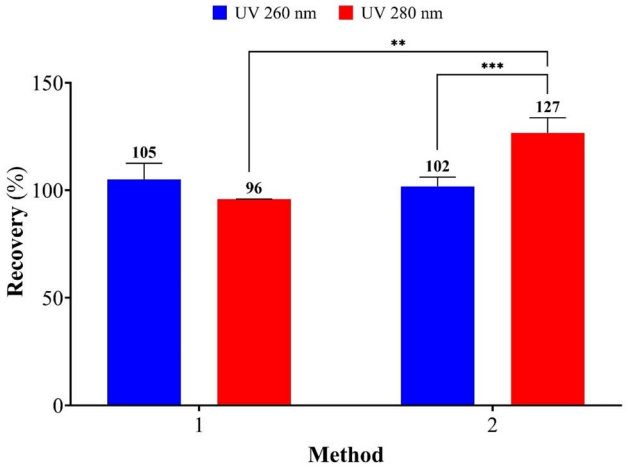

Fig. 6 Sample recovery of the LNP–BSA mixture incubated for 24-hour at 37 °C. Methods 1 and 2 have a cross-flow rate of 0.75 mL min^{-1} and 1.0 mL min^{-1} respectively. The detector flow rate for both methods is 0.2 mL min^{-1}. Statistical analysis was performed using one-way ANOVA followed by *post hoc* Tukey's test. Error bars represent ± SD mean of triplicate injections, $^{**}p < 0.01$, and $^{***}p < 0.001$.

dimensions[75] and sample viscosity[43] may also impact sample recovery. The analysis found that comparing methods 1 and 2 for the same wavelength with an increase in cross-flow rate, exhibited a non-significant reduction for 260 nm, but a significant increase for the 280 nm signal. Generally, higher cross-flow rates result in lower recovery rates, which may be explained by sample constituents being pushed close to the membrane by the channel perpendicular cross-flow, which increases interactions between sample analytes and the membrane.[43] This trend was observed with the UV 260 nm trace (Fig. 4D). The non-significant increase at 280 nm was attributed to increased saturation of the UV detector at 280 nm due to high BSA concentrations (35 mg mL^{-1}).

3.2.4 MALS scattering improves light-scattering model precision. The FI-AF4-MALS fractograms for the four methods are presented in Fig. 7. Coupling UV and MALS detectors to FI-AF4 enabled the detection of sub-populations eluting at identical retention times, indicating appropriate flow path alignment between detectors, and suggesting that methods 1–4 did not induce aggregation and exhibited minimal sample interaction with the FI-AF4 RC membrane. The principles underlying

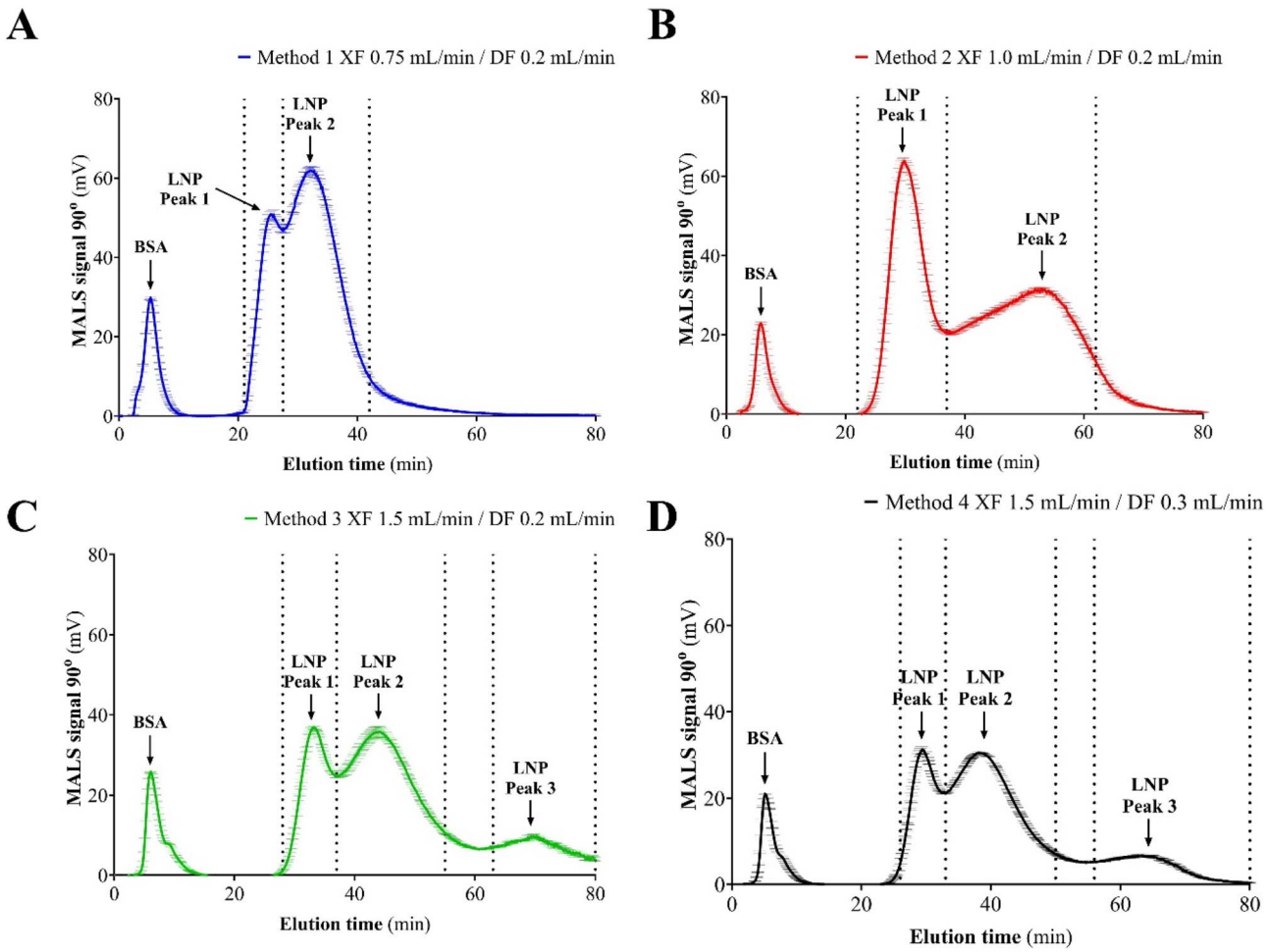

Fig. 7 FI-AF4-MALS fractograms for MC3-LNPs incubated in 35 mg mL^{-1} bovine serum albumin (BSA) for 24-hours at 37 °C. Methods 1–4 represent differences in the cross-flow rate (XF) and detector flow rate (DF). Plots represent (A) method 1, (B) method 2, (C) method 3 and (D) method 4. The peaks represent an initial bovine serum albumin (BSA) peak and peaks 1–3 represent different LNP sub-populations. Error bars represent ± SD mean of triplicate injections. Vertical dashed lines indicate the peak region of interest.

light scattering are well-established,[76,77] with scattered intensity directly related to the R_g of the particles. Accordingly, in the case of the LNP–BSA mixture, BSA, which has a smaller particle size as confirmed by batch-mode DLS (batch-mode DLS hydrodynamic diameter 7.5 (±0.2) nm) (Fig. 3A), exhibited lower light scattering intensity in comparison to larger-sized LNPs (batch-mode DLS hydrodynamic diameter 92.7 (±2.9) nm). Methods 1 and 2 yielded a monomodal peak for BSA indicating a homogeneous population. In contrast, methods 3 and 4, with a higher cross-flow rate of 1.5 mL min^{-1}, revealed two unresolved BSA sub-populations, consistent with the presence of oligomeric forms. These sub-populations were more clearly shown in the FI-AF4-MALS fractograms (Fig. 4 and 7). For LNPs, methods 3 and 4 indicated the presence of a third, higher-size sub-population (LNP peak 3) further demonstrating the resolving power of the FI-AF4-MALS approach.

Four different MALS scattering fit models were compared (Zimm, coated sphere, random coil and Debye) to determine the R_g for each nanoparticle fraction in the fractogram profile. The four fit models relate to the different relations of scattering intensity to $\sin^2(\theta/2)$.[78] Mathematical equations and first principles calculations for each mathematical transformation of R_g from the fit models are described elsewhere.[79] Fig. 8 shows MALS best fit models using two key statistical metrics, the coefficient of determination (R^2) and the root mean square error (RMSE).

R^2 measures the proportion of variance in the actual data that is explained by model predictions, with values closer to 1 indicating a stronger fit.[80] Conversely, RMSE quantifies the average magnitude of the prediction errors, representing how closely the predicted values match the observed measurements in absolute terms.[81] For the purpose of this study, the R^2 and RMSE were used to accurately characterise the R_g. Fig. 8 and SI Table S4 depicts the R_g as determined from light scattering data for Nova FFF software version 2.2.0.1 (Postnova Analytics, Landsberg, Germany) for each fitting method. The results suggest that BSA ($R_g \sim 4$–8 nm amongst all methods and model fits) has the least best-fit (R^2 ranging between 0.22–0.59) among the different fits and methods. Small molecules (<10 nm) have no angle-dependent light scattering, and scatter light isotropically, making it difficult to extract meaningful information about R_g even though the appropriate method parameters are chosen. The Zimm model fit for BSA and LNP peaks 1–3 demonstrated a zero gradient (Fig. 8 and SI Table S4), indicating

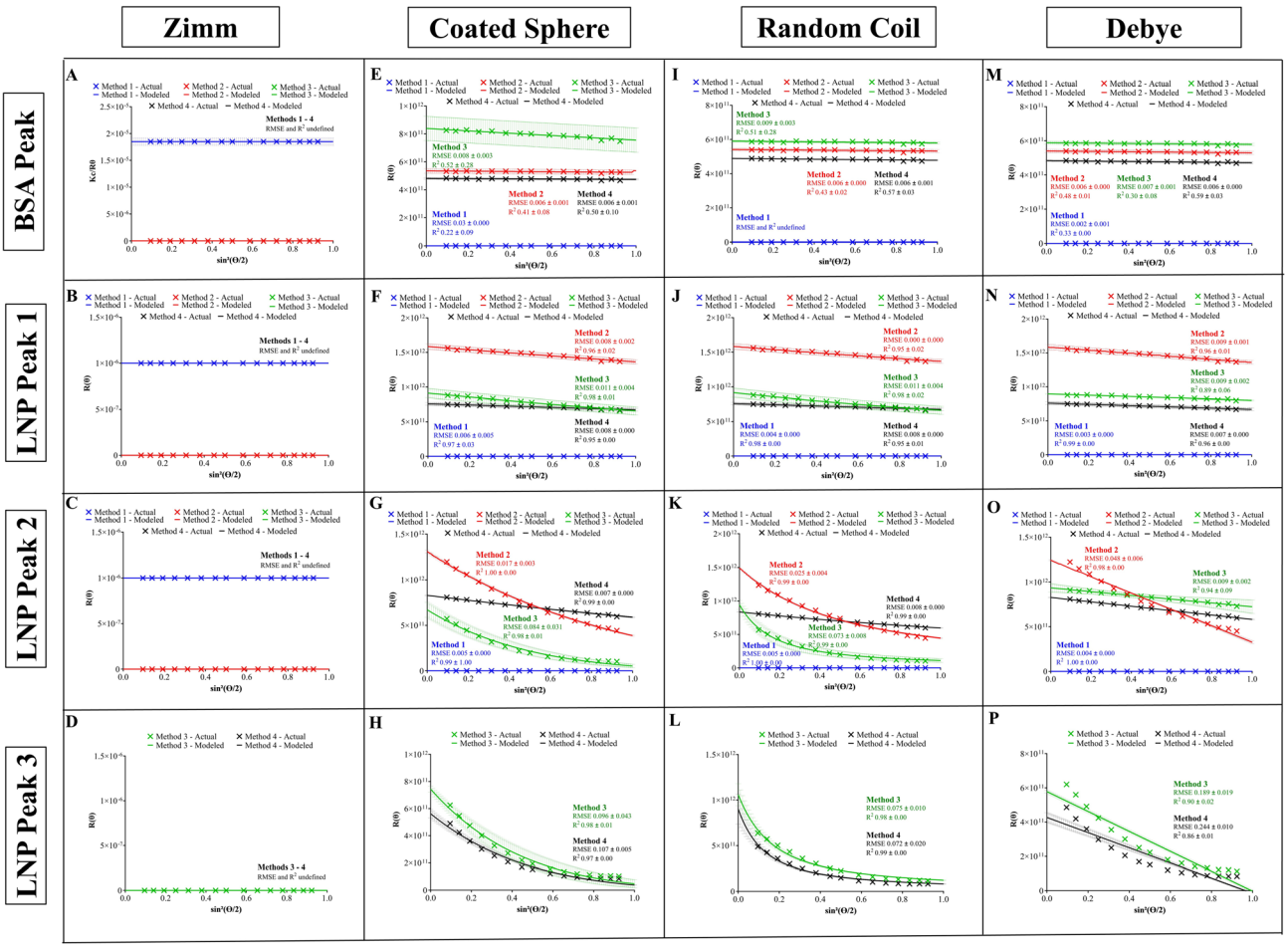

Fig. 8 Plots for the predicted and actual values for MALS scattering fit models (Zimm, coated sphere, random coil and Debye). Plots (A) to (D) represent the Zimm model, (E) to (H) coated sphere model, (I) to (L) random coil and (M) to (P) Debye model for BSA and LNP peaks 1–3. Refer to SI Table S4 for the coefficient of determination (R^2) and normalised root mean square error (RMSE) for the predicted and actual values.

that the scattering intensity is independent of the scattering angle. This exhibits unsuitability of the Zimm approximation for the LNP size. Therefore, the derived R_g for LNP sub-populations (peaks 1–3) for the Zimm model is unreliable. Furthermore, the RMSE for BSA using the coated sphere, random coil and Debye models resulted in a relatively low RMSE and low R^2. Hence, even though RMSE is low suggesting a low prediction error, the model may not capture variance in the data. Correlating the variance with FI-AF4, this can be attributed to the non-uniform flow profile of BSA where the BSA particles are interacting with the RC AF4 membrane.

For LNP peak 1, the coated sphere and the random coil had the highest R^2 and lowest normalised and RMSE values (R^2 0.95–0.98 and normalised RMSE 0.006–0.011 for coated sphere and R^2 0.95–0.98 and normalised RMSE 0.004–0.011 for random coil) (Fig. 8 and SI Table S4). This was comparable to LNP peak 2, which also resulted in the coated sphere and the random coil as best fits. For larger sized particles in the case of LNP peak 2, the coated sphere, random coil and Debye resulted in the highest R^2 (R^2 0.981, 0.976 and 0.932, respectively). Larger nanoparticles, in the case of LNP peak 3, had the lowest RMSE for the random coil fit (0.075 (±0.010) and 0.072 (±0.020) for method 3 and method 4, respectively).

In relation to comparing R_g between the different FI-AF4 methods (Fig. 9), method 4 having the highest cross-flow and the highest detector flow resulted in the largest R_g for BSA and LNP peaks 1–3. However, there was no trend of particle size with increased cross-flow (methods 1–3) for the same nanoparticle fraction. Method 2 has resulted in the largest R_g for both LNP peaks 1 and 2 (20.9 (±0.1) nm–21.4 (±0) nm for LNP peak 1 and 47.4 (±0.5) nm–72.7 (±1.3) nm for LNP peak 2).

Fig. 9 and SI Table S5 show an indirect correlation between the R_g and the cross-flow; the R_g does not increase with an increase in cross-flow. This is evident for all the methods among the coated sphere, random coil and Debye fit models. However, results show that an increase in detector flow results in an increase in R_g (method 3 *versus* method 4), which was consistent with coated sphere, random coil and Debye fit models (in the case of LNP peak 1, coated sphere model 31.1 (±0.7) nm for method 3 to 32.1 (±0.7) nm for method 4, random coil 18.1 (±0.8) nm method 3 to 19.9 (±0.3) nm method 4 and 17.6 (±0.7) nm to 19.2 (±0.3) nm). This can be attributed to the poor resolution in the separation of particles and a broader R_g with increased detector flow. Methods 3 and 4 (cross-flow of 1.5 mL min^{-1}) had higher fractionation power for the same elution profile as the other methods. Both methods resulted in the third LNP fraction (LNP peak 3) (>50 nm). Comparing all methods, the Debye model gave the lowest values of R_g for LNP peaks 1–3. The Debye model tends to underestimate R_g for particles >70 nm. This underestimation arises because the model assumptions do not adequately account for the structural complexities of larger particles.[82]

3.2.5 FI-AF4-DLS demonstrated significant differences in the hydrodynamic radius (R_h) among the four methods. The DLS detector (in flow-mode) coupled in-line to FI-AF4 provides a high resolution measurement of R_h for each component in a sample. The results obtained following fractionation in the channel revealed the presence of multiple size populations in-line with the fractograms for the MALS and UV detectors (Table 3 and SI Fig. S6). FI-AF4 multiplexed with MALS, UV and DLS detected sub-populations at the same elution time (Table 3). The R_h obtained by coupling FI-AF4 to DLS can be compared with batch-mode DLS for the BSA particle in the MC3-BSA mixture. In the case of batch-mode DLS, this has shown a single monomodal peak in the particle size distribution (R_h 3.8 (±0.2 nm)). In the case of FI-AF4 coupled to DLS, the broader distribution of R_h (methods 3 and 4 at a cross-flow of 1.5 mL min^{-1})

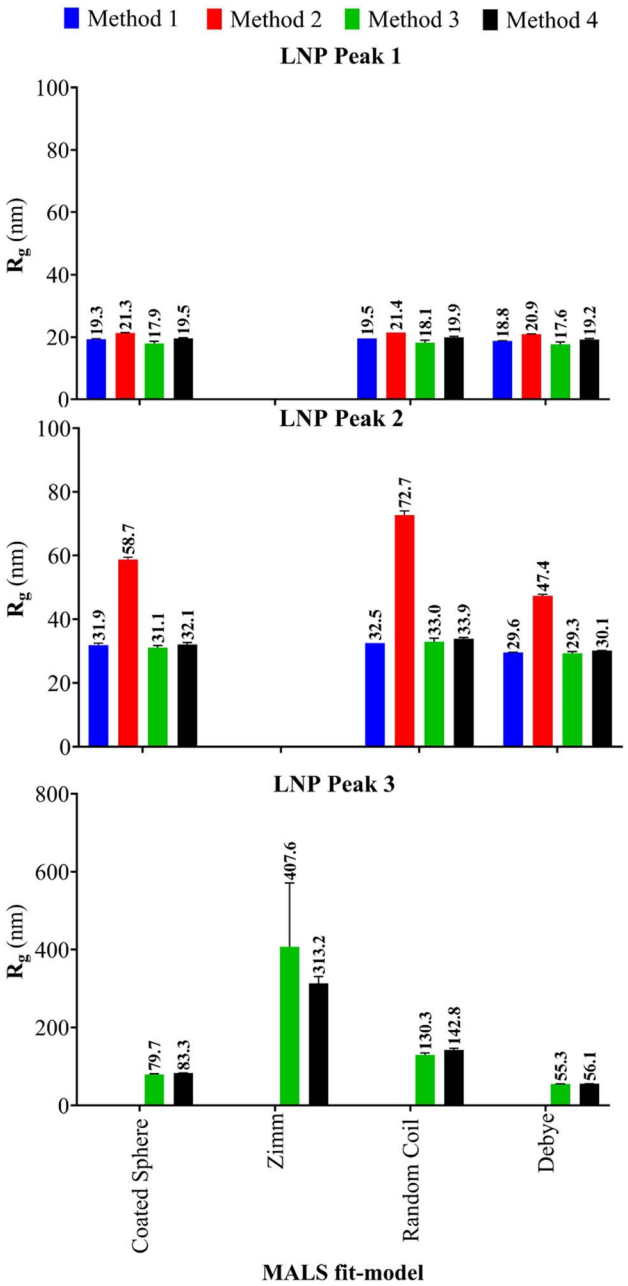

Fig. 9 Comparison of the radius of gyration (R_g) obtained from the different MALS fit models (coated sphere, Zimm, random coil and Debye) for FI-AF4 methods 1–4 for LNP peaks 1–3. Data are shown as ± SD mean of at least two injections. Refer to Fig. 7 for definition of the LNP peaks 1–3.

Table 3 Hydrodynamic radius (R_h) obtained from batch-mode dynamic light scattering (DLS) and FI-AF4 coupled to a DLS detector (FI-AF4-DLS) for methods 1–4. Data are shown as ± SD mean of 3 replicate injections ($n = 3$). A hyphen (—) indicates no peak identified

		Batch-mode DLS	FI-AF4-DLS			
			R_h (nm)			
			Method			
Sample	Constituents	R_h (nm)	1	2	3	4
MC3-BSA	BSA	3.8 (±0.2)	3.4 (±0.0)	3.4 (±0.0)	3.7 (±0.0)	4.2 (±0.1)
	LNP	46.4 (±2.9)	LNP peak 1	LNP peak 1	LNP peak 1	LNP peak 1
			25.3 (±0.1)	27.1 (±0.3)	24.3 (±0.1)	26.2 (±0.7)
			LNP peak 2	LNP peak 2	LNP peak 2	LNP peak 2
			38.4 (±0.2)	63.9 (±0.9)	40.0 (±0.2)	42.3 (±0.5)
			LNP peak 3	LNP peak 3	LNP peak 3	LNP peak 3
			—	—	71.1 (±2.0)	67.3 (±7.2)
	Aggregates	259.0 (±897.2)	—	—	—	—

for BSA suggests the resolving oligomeric forms. Similarly, whereas batch-mode DLS resulted in a single LNP peak at an R_h of 46.4 (±2.9) nm, in-line FI-AF4-DLS showed distinct populations of the LNPs in the LNP-BSA mixture. The R_h obtained for LNP peak 1 ranged between (24.3 (±0.1) nm to 27.1 (±0.3) nm), LNP peak 2 (38.4 (±0.2) nm to 63.9 (±0.9) nm) and LNP peak 3 (67.3 (±7.2) nm to 71.1 (±2.0) nm). Method 2 has resulted in the highest R_h compared to the other methods. This is similar to R_g for method 2 obtained using the MALS detector. Despite an increase in cross-flow between methods 1 to 3, there was no trend in the increase in R_h which was in line with results obtained for the R_g (Fig. 10). An increase in detector flow (methods 3 and 4) resulted in a significant increase in R_h for LNP peaks 1 and 2, but no significant decrease for LNP peak 3.

3.2.6 Combined contributions of FI-AF4 multiplexed with MALS and DLS for determining particle morphology. The combine use of both MALS and DLS detectors enables determination of particle morphology through calculation of the shape factor, defined as the ratio of R_g/R_h (eqn (3)). The effect of varying FI-AF4 parameters on the shape factor has not previously been reported. To gain insights into potential differences between shape factor values among different LNP sub-populations under different cross-flow and detector flow conditions, we evaluated the shape factor between distinct eluting sub-populations. R_g was extrapolated for the coated sphere fit model for light scattering data from the MALS detector for LNP peaks 1–3. The shape factor for an ideal sphere is ~0.77.[73] Oblong or rod-shaped particles have a ρ value of > 1.[83] We found significant differences in the shape factor values of each LNP subpopulation between different methods (Fig. 10 and SI Table S6). Shape factor values ranged between 0.709 and 0.793 (LNP peak 1), 0.765–0.853 (LNP peak 2) and 1.069–1.263 (LNP peak 3) (Fig. 10). The differences in the shape factor values between the different sample constituents can be attributed to the interaction of BSA with LNPs forming the protein corona.[30,84] A small increase in the shape factor typically suggests minimal protein

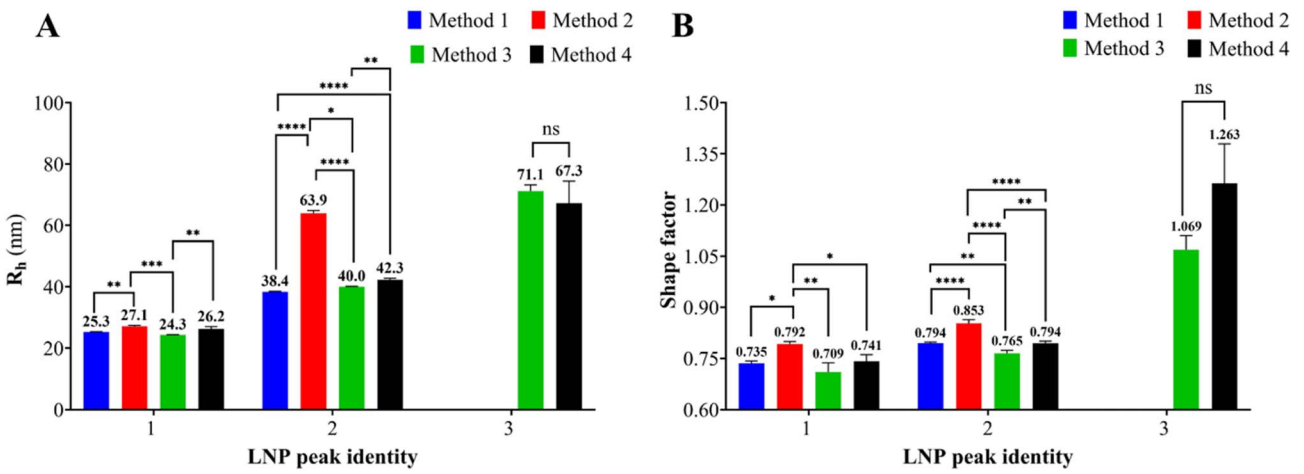

Fig. 10 Contribution of different detectors coupled to FI-AF4 for determining the (A) hydrodynamic radius (R_h) obtained by FI-AF4-DLS and (B) shape factor (R_g/R_h) obtained by FI-AF4-MALS-DLS. Characterisation was carried out for different sub-populations of LNPs (peak 1–3). Refer to SI Fig. S6 for DLS distribution plots and Fig. 7 for MALS (90°) signal and LNP peak identities. Statistical analysis of LNP peak 1 and peak 2 was performed using one-way ANOVA followed by *post hoc* Tukey's test. Statistical analysis of LNP peak 3 was carried out using the un-paired *t*-test. Error bars represent ± S.D mean of triplicate injections, *p < 0.05, **p < 0.01, ****p < 0.0001, and ns non-significant.

association with the nanoparticle surface, whereas a larger increase indicates substantial protein adsorption.[85] Fig. 10 shows that particle morphology is not constant amongst the different resolved sample sub-populations. Assuming BSA adsorption occurs at the surface of the LNP, the R_g increases more than the R_h leading to an elevated shape factor (0.765–0.853 (LNP peak 2) and 1.069–1.263 (LNP peak 3) compared to 0.709–0.793 (LNP peak 1)).

These findings indicate that the LNPs examined span a morphological spectrum ranging from coated spheres to rod-like structures, with measurable changes in morphology occurring throughout the FI-AF4 elution profile. The applied cross-flow and detector flow conditions in FI-AF4 altered nanoparticle morphology, likely due to particle alignment with flow and the force pushing particles towards the accumulation wall. The external forces and nanoparticle interactions with the accumulation wall and channel surfaces alter nanoparticle R_g and R_h, consequently altering the shape factor (R_g/R_h). Monitoring the shape factor is valuable, as it distinguishes the main particle population from additional sub-populations, such as aggregates or particles bearing a protein corona (shape factor > 0.77). The shape factor parameter also provides critical insights into formulation stability and biomolecular interactions that would not be apparent from particle size measurements alone. DLS and NTA used for the initial characterisation of the LNP sample did not provide information on the morphology or heterogeneity of the different sub-populations. In contrast, FI-AF4-MALS-DLS enabled assessment of particle morphology across the elution profile, as evidenced by analysis of the shape factor. Our previous work by Davidson *et al.*[86] and Roamcharern *et al.*,[87] established direct correlations between FI-AF4-derived shape factor (~0.7) values and particle morphologies determined by negative-stain transmission electron microscopy (TEM) and scanning electron microscopy (SEM) imaging, demonstrating strong agreement between AF4 measurements and imaging-based approaches. Marassi *et al.*,[88] similarly reported a shape factor value of 1.2 for aggregated human amniotic mesenchymal stromal cell-derived extracellular vesicles (hAMSC-EVs), further supporting the interpretation that elevated shape factor values are indicative of aggregated or non-spherical species.

4 Conclusions

In this study, we presented a detailed methodological and analysis framework for implementing FI-AF4 coupled to online detectors UV, MALS and DLS to separate and characterize polydisperse nanoparticle mixtures comprising LNPs and BSA. Our findings highlight the importance of careful method selection as a critical first step in bionanomaterial characterization, directly influencing the detector signal, resolution, light scattering model fit, and the accurate determination of particle size (R_g and R_h) and morphology (shape factor, R_g/R_h ratio). One of the key strengths of the FI-AF4 technique is its ability to resolve broad and heterogeneous particle size distributions, including the presence of large agglomerates, capabilities that outperform conventional analytical techniques. Particularly, methods employing elevated cross-flow rates improved the resolution of larger agglomerates, further highlighting advantages of FI-AF4 for analysing complex mixtures. Accurate interpretation of AF4-MALS data requires careful selection and reporting of the appropriate light-scattering model, as the choice of fit substantially affects calculated parameters such as R_g and the resulting shape factor. While the results presented here focus on LNPs and proteins, the workflow and analytical considerations described are broadly applicable to a wide range of heterogeneous nanoparticle systems. Moreover, we emphasize the importance of extracting and critically evaluating raw AF4 data to guide robust method development and improve reproducibility in the characterization of complex bionanomaterials.

Author contributions

Conceptualization: ZR; methodology, formal analysis, investigation, data curation, writing – original draft preparation, writing – reviewing and editing, visualisation: RA, PP, LvD, NJWR, RC, KT, YP, and ZR; supervision: ZR, KT, RC, and YP; project administration, funding acquisition: KT and ZR. All authors have read and agreed to the published version of the manuscript.

Conflicts of interest

The authors declare the following financial interests/personal relationships, which may be considered as potential competing interests: Zahra Rattray reports that financial support was provided by AstraZeneca UK Limited. Zahra Rattray reports that financial support was provided by Engineering and Physical Sciences Research Council. Robin Capomaccio and Kevin Treacher report a relationship with AstraZeneca UK Limited that includes employment and stock ownership. If there are other authors, they declare that they have no known competing financial interests or personal relationships that could have appeared to influence the work reported in this paper.

Data availability

All data associated with this manuscript are available as a downloadable dataset from https://doi.org/10.15129/e36c85bc-a7a1-48d1-8c0c-7ee53b4d1e61.

Supplementary information (SI) is available. See DOI: https://doi.org/10.1039/d5ay01758k.

Acknowledgements

This work was supported by the UK Engineering and Physical Sciences Research Council (ZR, EPSRC EP/V028960/1). We acknowledge funding from AstraZeneca Pharmaceuticals for RA's PhD scholarship.

References

1 EMA, *Onpattro Assessment Report*, 2018.

2 National Center for Immunization and Respiratory Diseases, *Moderna COVID-19 Vaccine (Also Known as Spikevax) Overview and Safety*, National Center for Immunization and Respiratory Diseases, USA, 2022.
3 Moderna TX, Inc., *FDA Approval Letter - mNEXSPIKE*, U.S. FDA, 2025.
4 EMA, *Comirnaty - Summary of Product Characteristics*, 2020.
5 ACIP, *Grading of Recommendations, Assessment, Development, and Evaluation (GRADE): Moderna mRNA RSV Vaccine (mResvia) in Older Adults*, 2024.
6 S. C. Semple, *et al.*, Rational design of cationic lipids for siRNA delivery, *Nat. Biotechnol.*, 2010, **28**(2), 172–176.
7 S. Patel, *et al.*, Naturally-occurring cholesterol analogues in lipid nanoparticles induce polymorphic shape and enhance intracellular delivery of mRNA, *Nat. Commun.*, 2020, **11**(1), 983.
8 L. Zhang, *et al.*, Role of PEGylated lipid in lipid nanoparticle formulation for in vitro and in vivo delivery of mRNA vaccines, *J. Controlled Release*, 2025, **380**, 108–124.
9 J. E. C. P. Payne, *Ionizable Cationic Lipid for RNA Delivery*, Arcturus Therapeutics, Inc., United States, 2017.
10 A. Borah, *et al.*, From in vitro to in Vivo: The Dominant role of PEG-Lipids in LNP performance, *Eur. J. Pharm. Biopharm.*, 2025, 114726.
11 M. Hussain, *et al.*, Mind the Age Gap: Expanding the Age Window for mRNA Vaccine Testing in Mice, *Vaccines*, 2025, **13**(4), 370.
12 J. A. Kulkarni, *et al.*, On the role of helper lipids in lipid nanoparticle formulations of siRNA, *Nanoscale*, 2019, **11**(45), 21733–21739.
13 O. A. Smith, *et al.*, Impact of Metabolic States on SARS-CoV-2 Vaccine Responses in Mouse Models of Obesity and Diabetes, *COVID*, 2025, **5**(1), 2.
14 J. G. Rurik, *et al.*, CAR T cells produced in vivo to treat cardiac injury, *Science*, 2022, **375**(6576), 91–96.
15 T. Nakamura, *et al.*, The Effect of Size and Charge of Lipid Nanoparticles Prepared by Microfluidic Mixing on Their Lymph Node Transitivity and Distribution, *Mol. Pharm.*, 2020, **17**(3), 944–953.
16 K. Lee, *et al.*, Adjuvant incorporated lipid nanoparticles for enhanced mRNA-mediated cancer immunotherapy, *Biomater. Sci.*, 2020, **8**(4), 1101–1105.
17 L. Miao, *et al.*, Delivery of mRNA vaccines with heterocyclic lipids increases anti-tumor efficacy by STING-mediated immune cell activation, *Nat. Biotechnol.*, 2019, **37**(10), 1174–1185.
18 Y. Zhang, *et al.*, STING Agonist-Derived LNP-mRNA Vaccine Enhances Protective Immunity Against SARS-CoV-2, *Nano Lett.*, 2023, **23**(7), 2593–2600.
19 E. N. C. Laboratory, *FFF-MALS Method Development and Measurements of Size and Molecular Weight*, 2016.
20 E. C. F. Standardization, *Nanotechnologies — Analysis of Nano-Objects Using Asymmetrical-Flow and Centrifugal Field-Flow Fractionation*, 2021.
21 A. S. F. T. Materials, *Standard Practice for Workforce Education in Nanotechnology Characterization*, 2020.
22 F. Caputo, *et al.*, Toward an international standardisation roadmap for nanomedicine, *Drug Delivery Transl. Res.*, 2024, **14**(9), 2578–2588.
23 G. Guerrini, *et al.*, Characterization of nanoparticles-based vaccines for COVID-19, *Nat. Nanotechnol.*, 2022, **17**(6), 570–576.
24 J. Forrester, *et al.*, Low-Cost Microfluidic Mixers: Are They up to the Task?, *Pharmaceutics*, 2025, **17**(5), 566.
25 P. S. Fedotov, *et al.*, Fractionation and characterization of nano- and microparticles in liquid media, *Anal. Bioanal. Chem.*, 2011, **400**(6), 1787–1804.
26 J. Kuntsche, C. Decker and A. Fahr, Analysis of liposomes using asymmetrical flow field-flow fractionation: separation conditions and drug/lipid recovery, *J. Sep. Sci.*, 2012, **35**(15), 1993–2001.
27 S. Hupfeld, D. Ausbacher and M. Brandl, Asymmetric flow field-flow fractionation of liposomes: 2. Concentration detection and adsorptive loss phenomena, *J. Sep. Sci.*, 2009, **32**(20), 3555–3561.
28 C. Decker, *et al.*, Selective partitioning of cholesterol and a model drug into liposomes of varying size, *Chem. Phys. Lipids*, 2012, **165**(5), 520–529.
29 C. L. Plavchak, *et al.*, Utilization of AF4 for characterizing complex nanomaterial drug products: Reexamining sample recovery and its impact on particle size distribution as a quality attribute, *J. Chromatogr. A*, 2025, **1743**, 465703.
30 R. Abdulrahman, *et al.*, Frit-inlet asymmetric flow field-flow fractionation for the analysis of lipid nanoparticle-protein interactions, *J. Chromatogr. A*, 2025, **1743**, 465663.
31 M. Hansen and J. D. Clogston, Nanoparticle Size Distribution and Stability Assessment Using Asymmetric-Flow Field-Flow Fractionation, *Methods Mol. Biol.*, 2024, **2789**, 21–29.
32 M. S. Bohsen, *et al.*, Interaction of liposomes with bile salts investigated by asymmetric flow field-flow fractionation (AF4): A novel approach for stability assessment of oral drug carriers, *Eur. J. Pharm. Sci.*, 2023, **182**, 106384.
33 J. C. Giddings, Field-flow fractionation: analysis of macromolecular, colloidal, and particulate materials, *Science*, 1993, **260**(5113), 1456–1465.
34 X. Jia, *et al.*, Enabling online determination of the size-dependent RNA content of lipid nanoparticle-based RNA formulations, *J. Chromatogr. B:Anal. Technol. Biomed. Life Sci.*, 2021, **1186**, 123015.
35 J. C. Giddings, A new separation concept based on a coupling of concentration and flow nonuniformities, *Sep. Sci.*, 1966, **1**(1), 123–125.
36 M. H. Moon, H. Kwon and I. Park, Stopless flow injection in asymmetrical flow field-flow fractionation using a frit inlet, *Anal. Chem.*, 1997, **69**(7), 1436–1440.
37 C. Fuentes, *et al.*, Comparison between conventional and frit-inlet channels in separation of biopolymers by asymmetric flow field-flow fractionation, *Analyst*, 2019, **144**(15), 4559–4568.
38 Y. P. Chuan, *et al.*, Quantitative analysis of virus-like particle size and distribution by field-flow fractionation, *Biotechnol. Bioeng.*, 2008, **99**(6), 1425–1433.

39 G. Yohannes, *et al.*, Asymmetrical flow field-flow fractionation technique for separation and characterization of biopolymers and bioparticles, *J. Chromatogr. A*, 2011, **1218**(27), 4104–4116.
40 R. Mildner, *et al.*, Improved multidetector asymmetrical-flow field-flow fractionation method for particle sizing and concentration measurements of lipid-based nanocarriers for RNA delivery, *Eur. J. Pharm. Biopharm.*, 2021, **163**, 252–265.
41 L. M. F. Ramirez, *et al.*, Characterization of dextran particle size: How frit-inlet asymmetrical flow field-flow fractionation (FI-AF4) coupled online with dynamic light scattering (DLS) leads to enhanced size distribution, *J. Chromatogr. A*, 2021, **1653**, 462404.
42 C. G. Davidson, *et al.*, The use of orthogonal analytical approaches to profile lipid nanoparticle physicochemical attributes, *Nano Futures*, 2024, **8**(3), 035001.
43 M. Marioli and W. T. Kok, Recovery, overloading, and protein interactions in asymmetrical flow field-flow fractionation, *Anal. Bioanal. Chem.*, 2019, **411**(11), 2327–2338.
44 R. Gasco, *et al.*, Asymmetric flow field-flow fractionation for comprehensive characterization of hetero-aggregates made of nano-silver and extracellular polymeric substances, *J. Chromatogr. A*, 2025, **1739**, 465507.
45 F. Caputo, *et al.*, Asymmetric-flow field-flow fractionation for measuring particle size, drug loading and (in)stability of nanopharmaceuticals. The joint view of European Union Nanomedicine Characterization Laboratory and National Cancer Institute - Nanotechnology Characterization Laboratory, *J. Chromatogr. A*, 2021, **1635**, 461767.
46 R. Abdulrahman, P. Punnabhum, R. Capomaccio, K. Treacher, Y. Perrie and Z. Rattray, Frit-inlet asymmetric flow field-flow fractionation for the analysis of lipid nanoparticle-protein interactions, *J. Chromatogr. A*, 2025, **1743**, 465663.
47 C. L. Plavchak, *et al.*, Determination of particle number concentration for biological particles using AF4-MALS: Dependencies on light scattering model and refractive index, *J. Chromatogr. A*, 2024, **1737**, 465460.
48 S. Shakiba, *et al.*, Asymmetric flow field-flow fractionation (AF4) with fluorescence and multi-detector analysis for direct, real-time, size-resolved measurements of drug release from polymeric nanoparticles, *J. Controlled Release*, 2021, **338**, 410–421.
49 F. Caputo, *et al.*, Measuring Particle Size Distribution by Asymmetric Flow Field Flow Fractionation: A Powerful Method for the Preclinical Characterization of Lipid-Based Nanoparticles, *Mol. Pharm.*, 2019, **16**(2), 756–767.
50 J. Parot, *et al.*, Quality assessment of LNP-RNA therapeutics with orthogonal analytical techniques, *J. Controlled Release*, 2024, **367**, 385–401.
51 C. Hiemenz, *et al.*, Characterization of Virus Particles and Submicron-Sized Particulate Impurities in Recombinant Adeno-Associated Virus Drug Product, *J. Pharm. Sci.*, 2023, **112**(8), 2190–2202.
52 I. K. Ventouri, *et al.*, Characterizing Non-covalent Protein Complexes Using Asymmetrical Flow Field-Flow Fractionation On-Line Coupled to Native Mass Spectrometry, *Anal. Chem.*, 2023, **95**(19), 7487–7494.
53 A. Boughbina-Portoles, *et al.*, Reliable assessment of carbon black nanomaterial of a variety of cell culture media for in vitro toxicity assays by asymmetrical flow field-flow fractionation, *Anal. Bioanal. Chem.*, 2023, **415**(11), 2121–2132.
54 B. Moreira-Alvarez, *et al.*, AF4-UV/VIS-MALS-ICPMS/MS for the characterization of the different nanoparticulated species present in oligonucleotide-gold nanoparticle conjugates, *Talanta*, 2023, **256**, 124309.
55 F. Geissler, *et al.*, Optimization of hyphenated asymmetric flow field-flow fractionation for the analysis of silver nanoparticles in aqueous solutions, *Anal. Bioanal. Chem.*, 2021, **413**(27), 6889–6904.
56 M. Klein, *et al.*, Advanced nanomedicine characterization by DLS and AF4-UV-MALS: Application to a HIV nanovaccine, *J. Pharm. Biomed. Anal.*, 2020, **179**, 113017.
57 T. W. Hsu, *et al.*, Revealing cholesterol effects on PEGylated HSPC liposomes using AF4-MALS and simultaneous small- and wide-angle X-ray scattering, *J. Appl. Crystallogr.*, 2023, **56**(Pt 4), 988–993.
58 A. Sajid, M. Castronovo and F. M. Goycoolea, On the Fractionation and Physicochemical Characterisation of Self-Assembled Chitosan-DNA Polyelectrolyte Complexes, *Polymers*, 2023, **15**(9), 2115.
59 Y. Gonzalez-Espinosa, *et al.*, Characterisation of chitosan molecular weight distribution by multi-detection asymmetric flow-field flow fractionation (AF4) and SEC, *Int. J. Biol. Macromol.*, 2019, **136**, 911–919.
60 A. C. Makan, *et al.*, Advanced analysis of polymer emulsions: Particle size and particle size distribution by field-flow fractionation and dynamic light scattering, *J. Chromatogr. A*, 2016, **1442**, 94–106.
61 C. R. M. Bria, *et al.*, Asymmetrical flow field-flow fractionation for improved characterization of human plasma lipoproteins, *Anal. Bioanal. Chem.*, 2019, **411**(3), 777–786.
62 C. R. Bria and S. K. Williams, Impact of asymmetrical flow field-flow fractionation on protein aggregates stability, *J. Chromatogr. A*, 2016, **1465**, 155–164.
63 W. Burchard, M. Schmidt and W. Stockmayer, Information on polydispersity and branching from combined quasi-elastic and intergrated scattering, *Macromolecules*, 1980, **13**(5), 1265–1272.
64 B. M. Tande, *et al.*, Viscosimetric, hydrodynamic, and conformational properties of dendrimers and dendrons, *Macromolecules*, 2001, **34**(24), 8580–8585.
65 Y. Chen, *et al.*, Asymmetrical flow field-flow fractionation coupled with multi-angle laser light scattering for stability comparison of virus-like particles in different solution environments, *Vaccine*, 2016, **34**(27), 3164–3170.
66 I. V. Safenkova, *et al.*, Complex analysis of concentrated antibody-gold nanoparticle conjugates' mixtures using

asymmetric flow field-flow fractionation, *J. Chromatogr. A*, 2016, **1477**, 56–63.
67 C.-H. Shen, Chapter 7 - Quantification and analysis of nucleic acids, in *Diagnostic Molecular Biology*, ed. C.-H. Shen, Academic Press, 2nd edn, 2023. pp. 181–208.
68 M. H. Simonian, Spectrophotometric determination of protein concentration, *Curr. Protoc. Cell Biol.*, 2002, **3**, 3B.
69 K. D. Caldwell, *et al.*, Sample overloading effects in polymer characterization by field-flow fractionation, *J. Appl. Polym. Sci.*, 1988, **36**(3), 703–719.
70 C. Arfvidsson and K. G. Wahlund, Mass overloading in the flow field-flow fractionation channel studied by the behaviour of the ultra-large wheat protein glutenin, *J. Chromatogr. A*, 2003, **1011**(1–2), 99–109.
71 J. E. Wijnhoven, *et al.*, Influence of injected mass and ionic strength on retention of water-soluble polymers and proteins in hollow-fibre flow field-flow fractionation, *J. Chromatogr. A*, 1996, **732**(2), 307–315.
72 P. Debye, Molecular-weight Determination by Light Scattering, *J. Phys. Colloid Chem.*, 1947, **51**(1), 18–32.
73 Y. Hu, R. M. Crist and J. D. Clogston, The utility of asymmetric flow field-flow fractionation for preclinical characterization of nanomedicines, *Anal. Bioanal. Chem.*, 2020, **412**(2), 425–438.
74 K. Reinmuth-Selzle, *et al.*, Determination of the protein content of complex samples by aromatic amino acid analysis, liquid chromatography-UV absorbance, and colorimetry, *Anal. Bioanal. Chem.*, 2022, **414**(15), 4457–4470.
75 C. R. M. Bria, *et al.*, Semi-preparative asymmetrical flow field-flow fractionation: A closer look at channel dimensions and separation performance, *J. Chromatogr. A*, 2017, **1499**, 149–157.
76 D. Roessner and W.-M. Kulicke, On-line coupling of flow field-flow fractionation and multi-angle laser light scattering, *J. Chromatogr. A*, 1994, **687**(2), 249–258.
77 C. F. Bohren and D. R. Huffman, *Absorption and Scattering of Light by Small Particles*, John Wiley & Sons, 2008.
78 M. Andersson, B. Wittgren and K. G. Wahlund, Accuracy in multiangle light scattering measurements for molar mass and radius estimations. Model calculations and experiments, *Anal. Chem.*, 2003, **75**(16), 4279–4291.
79 M. Baalousha, *et al.*, Size fractionation and characterization of natural colloids by flow-field flow fractionation coupled to multi-angle laser light scattering, *J. Chromatogr. A*, 2006, **1104**(1–2), 272–281.
80 O. Renaud and M.-P. Victoria-Feser, A robust coefficient of determination for regression, *J. Stat. Plan. Infer.*, 2010, **140**(7), 1852–1862.
81 J. Nevitt and G. R. Hancock, Improving the Root Mean Square Error of Approximation for Nonnormal Conditions in Structural Equation Modeling, *J. Exp. Edu.*, 2000, **68**(3), 251–268.
82 C. S. Hundschell, F. Jakob and A. M. Wagemans, Molecular weight dependent structure of the exopolysaccharide levan, *Int. J. Biol. Macromol.*, 2020, **161**, 398–405.
83 J. Lohrke, A. Briel and K. Mader, Characterization of superparamagnetic iron oxide nanoparticles by asymmetrical flow-field-flow-fractionation, *Nanomedicine*, 2008, **3**(4), 437–452.
84 S. V. Patil, D. M. Lee, B. R. Ratna, K. Ahmed, E. M. Kennedy and S. E. McNeil, *Characterization of Nanoparticles Intended for Drug Delivery*, Humana Press, Springer, 2011, vol. 697.
85 M. Hansen and J. D. Clogston, Assessment of Protein Binding Using Asymmetric-Flow Field-Flow Fractionation Combined with Multi-angle Light Scattering and Dynamic Light Scattering, *Methods Mol. Biol.*, 2024, **2789**, 31–34.
86 C. G. Davidson, *et al.*, The Use of Enhanced Analytical Pipelines for the Characterization of Poly(A) and Poly(A)-LNP Formulation Critical Quality Attributes, *Mol. Pharmaceutics*, 2025, **22**(12), 7383–7399.
87 N. Roamcharern, *et al.*, Evaluating the impact of bioinspired counterion inclusion on silk nanoparticle physicochemical attributes and physical stability, *Nanoscale Adv.*, 2025, **7**(18), 5519–5535.
88 V. Marassi, *et al.*, Native characterization and QC profiling of human amniotic mesenchymal stromal cell vesicular fractions for secretome-based therapy, *Talanta*, 2024, **276**, 126216.